LANGMUIR

pubs.acs.org/Langmuir Article

Liquid Transfer for Viscoelastic Solutions

Hrishikesh Pingulkar, Jorge Peixinho,* and Olivier Crumeyrolle

Cite This: *Langmuir* 2021, 37, 10348−10353 Read Online

ACCESS | Metrics & More | Article Recommendations | Supporting Information

ABSTRACT: Viscoelastic liquid transfer from one surface to another is a process that finds applications in many technologies, primarily in printing. Here, cylindrical-shaped capillary bridges pinned between two parallel disks are considered. Specifically, the effects of polymer mass fraction, solution viscosity, disk diameter, initial aspect ratio, final aspect ratio, stretching velocity, and filling fraction (alike contact angle) are experimentally investigated in uniaxial extensional flow. Both Newtonian and viscoelastic polymer solutions are prepared using polyethylene glycol and polyethylene oxide, with a wide variety of mass fractions. The results show that the increase in polymer mass fraction and solvent viscosity reduces the liquid transfer to the top surface. Moreover, the increase in the initial and final stretching heights of the capillary bridge also decreases the liquid transfer for both Newtonian and viscoelastic solutions. Finally, the shape of the capillary bridge is varied by changing the liquid volume. Now, Newtonian and viscoelastic solutions exhibit opposite behaviors for the liquid transfer. These findings are discussed in terms of interfacial shape instability and gravitational drainage.

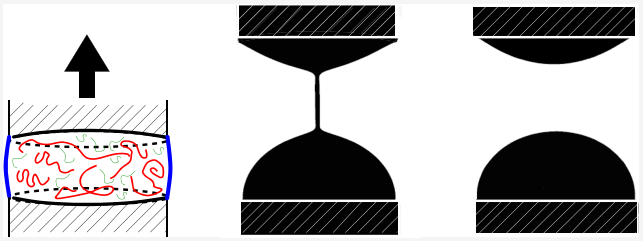

INTRODUCTION

Liquid capillary bridges can be found in many industrial applications such as food processing, material engineering, adhesion processes, coating technology, flow in porous media, microfluidics, and measurements of rheological properties.[1−4] One of the motivations for the study of stretched liquid bridges is its close association with printing processes. Nowadays, a printing process not only is limited to books, magazines, and newspapers but also has expanded to various areas like manufacturing of electric circuits,[1] printed wearable electronics,[5] screen displays, lab-on-a-chip,[6] solar cells,[7] and 3D microstructures (polymer wires, needles, pillars, cones, and microspheres).[8] The printing industry deals with inks, which can contain polymers, surfactants, or particles and have viscoelastic properties. While printing, the liquid from one surface is transferred to another surface through the formation of a capillary liquid bridge. For Newtonian fluids, during this liquid transfer, solution pools are formed on the end plates of a stretched liquid bridge. On the other hand, a stretched viscoelastic liquid bridge forms a persistent thin filament[9−14] along with the solution pools.

Due to complexities involving surface and liquid properties as well as the formation of filaments, the transfer of the desired volume of liquid is a challenge in the printing industry. Specifically, capillary, viscous, inertial, elastic, and gravitational forces all play a role in this liquid transfer. A relevant parameter called the transfer ratio, T_r, is defined as the fraction of liquid transferred to the moving disk (accepter) to the total amount of liquid left on both disks, as shown in Figure 1. The geometrical properties that affect T_r are the disk radius, R_0, or

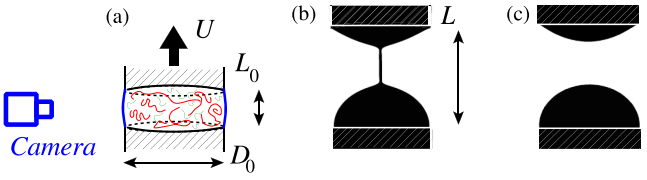

Figure 1. (a) Liquid capillary bridge of the polymer solution sandwiched between parallel disks of diameter D_0 and initial height L_0 before being stretched with a velocity, U. (b) The top disk reaches the final stretching height, L, and a thinning filament is observed. (c) Breakup of the liquid bridge.

the disk diameter, D_0, the stretching speed, U, the initial aspect ratio, L_0/R_0, and the final aspect ratio, L/R_0.

Chadov and Yakhnin[15,16] first identified the liquid-transfer phenomenon for several liquids of viscosity η and surface tension σ on various surfaces. In their experiments, the top flat surface was brought downward to press a liquid drop on the bottom surface and then moved upward to stretch the capillary bridge at high capillary numbers, that is, $Ca = \eta U/\sigma > 1$. Under these conditions, the liquid transfer is independent of surface and liquid properties, which was later confirmed by others authors.[17−20] Noteworthily, when the contact angles on both plates are 45°, T_r is found to be 0.5.

Received: June 1, 2021
Revised: August 5, 2021
Published: August 18, 2021

https://doi.org/10.1021/acs.langmuir.1c01462
Langmuir 2021, 37, 10348−10353

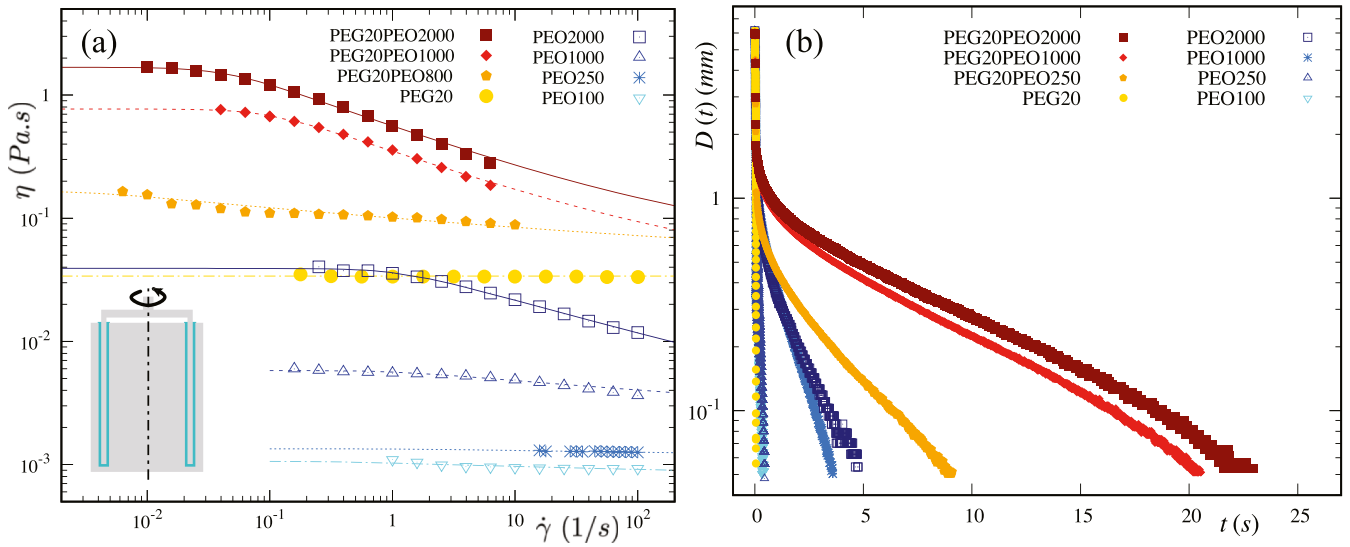

Figure 2. (a) Steady shear viscosity against shear rate and (b) diameter time evolution for aqueous solutions of PEO, PEG, and PEG20PEO. The inset in (a) is a sketch of the double-wall geometry (drawn up to scale) used, and the lines represent fits described in the text.

The issues of wetting and the dynamic contact angle[21] are generally avoided by pinning the contact line to the edge of a disk. For example, Zhang et al.[22] investigated, theoretically and experimentally, the stability and breakup of the liquid bridge, with fixed contact lines at the edges. The authors found that T_r decreases with increasing disk diameter but increases with the stretching speed. In practice, gravure cells are used[23−26] to control the ink spreading. The effect of viscoelastic polymer solutions on T_r for the gravure printing is studied experimentally by Sankaran and Rothstein[25] and numerically by Lee et al.[26] In the beginning, the liquid transfer is governed by the early stretching dynamics, while the final amount of liquid transfer occurs through the delayed viscoelastic filament thinning.[25−27] In contrast, the present study focuses on the cylindrical-shaped liquid bridges, with the pinned contact lines on disks to overcome the shearing effect.[27]

In the present paper, our experimental study mainly focuses on T_r for a cylindrical-shaped bridge of viscoelastic as well as Newtonian fluids. Solutions will be prepared by varying the mass fraction and molecular weight of polymers to investigate the effect of viscoelasticity on liquid transfer. The same stainless-steel disks at the top and bottom will be used to overcome the complexities due to different surface materials as previously reported.[15,16,27] Different disk diameters, initial and final aspect ratios, and the initial profile curvatures are explored.

MATERIALS AND METHODS

Sample Preparation. Aqueous solutions of poly-ethylene oxide (PEO), which is a high-molecular-weight polymer, and poly-ethylene glycol (PEG), which has a relatively low molecular weight, are used either separately or in combination. PEO solutions are commonly used to investigate viscoelastic behavior of liquid jets,[28,29] beads on a string,[10,14,30,31] coatings,[32−34] and liquid transfer.[25,27] Broadly, our strategy is to control the shear viscosity with PEG and the extensional viscosity with the mass fraction of PEO. The molecular weight of PEO is 8×10^6 g/mol and the molecular weight of PEG is 20,000 g/mol according to Sigma-Aldrich. Three different types of solutions are prepared: (i) aqueous PEG solutions, (ii) aqueous PEO solutions, and (iii) mixtures of PEG and PEO solutions. For the solutions containing PEO, 0.5 wt % iso-propyl alcohol is added for easy dispersion of PEO molecules in the solvent.[35] The mass fraction of PEO in solutions ranges from 100 to 2000 ppm with and without PEG. Note that a solution of 1000 ppm of PEO is labeled as PEO1000. Similarly, a solution of 20 wt % PEG and 2000 ppm of PEO is labeled as PEG20PEO2000. The density, ρ, and σ were measured for each solution, and the values are reported in Table S1 in the Supporting Information.

Rheological Measurements. The shear viscosity of the solutions was measured using a rotating rheometer (TA Instruments Discovery HR-3) with a double-wall concentric cylinder geometry. High-polymer-mass-fraction solutions exhibit shear thinning, as shown in Figure 2a. The zero shear viscosity, η_0, was obtained from fitting the Carreau equation[36] with the infinite viscosity prescribed to the solvent one.

Additional rheological measurements were conducted using a capillary breakup extensional rheometer (CaBER from Thermo Haake). The filament diameter around mid-height is tracked over the time using an in-built laser (see Figure 2b). The diameter decreases with time for all solutions. For viscoelastic solutions, the diameter exhibits an exponential thinning, characterized by the extensional relaxation time, λ. Further analysis of the diameter can be used to obtain the extensional viscosity as a function of time and Hencky strain. These results are given in Pingulkar et al.[14]

Based on the solution properties, several dimensionless numbers can be defined. The Deborah number, $De = \lambda/\tau_R$, represents a ratio of the viscoelastic time, λ, to the Rayleigh inertio-capillary time: $\tau_R = \sqrt{\rho {R_0}^3/\sigma}$. Other authors[26,37] use the ratio λ/τ_v with the viscous time $\tau_v = \eta_0 R_0/\sigma$. In addition, the ratio of the viscous and Rayleigh times is also needed, that is, the Ohnesorge number: $Oh = \tau_v/\tau_R$. Another important number to characterize a capillary bridge is the Bond number quantifying the effect of gravitational to capillary forces: $Bo = \rho g {R_0}^2/\sigma$. Later, when the capillary bridge shape is non-cylindrical, the mid-height radius, R_{mid}, will be used, leading to Bo_m. The experiments use three disk diameters and additional mass fractions, and parameters are presented in Table S2 in the Supporting Information.

Experimental Setup. The capillary bridge stretching is studied experimentally with the CaBER and a high-speed camera (800 × 1280 pixels). The resolution for typical experiments is 1 pixel = 2 μm. Shadowgraphic images are obtained using a continuous laser and a diffuser (from Dantec Dynamics). Initially, a liquid capillary bridge is created by placing a solution sample in between the two parallel disks. The volume of the solution introduced in the liquid bridge depends on R_0 and the initial height, L_0, and this volume is calculated as $\mathcal{V} = \pi L_0 {R_0}^2$. The liquid volume introduced is controlled with the

https://doi.org/10.1021/acs.langmuir.1c01462
Langmuir 2021, 37, 10348−10353

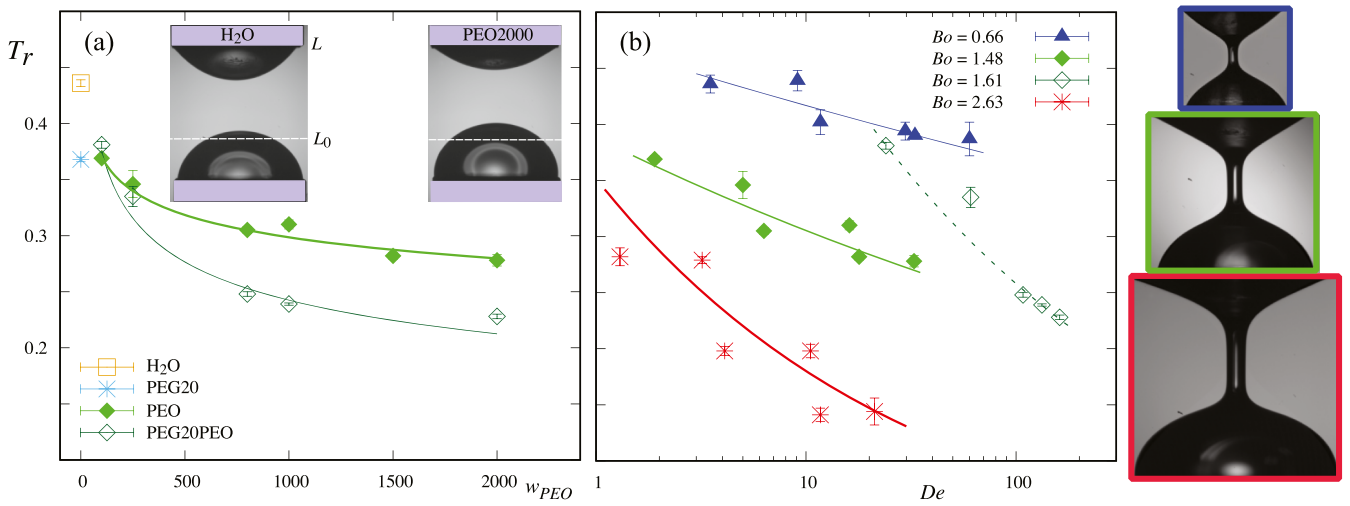

Figure 3. (a) Transfer ratio, T_r, as a function of the polymer mass fraction, w_{PEO}. R_0 = 3 mm, L_0/R_0 = 0.66, and L/R_0 = 2 at U = 0.08 m/s. (b) Transfer ratio, T_r, as a function of De for different Bo. The insets are stretched liquid bridges for 1000 ppm of PEO for R_0 = 2, 3, and 4 mm (from top to bottom).

help of a pipette (Eppendorf research plus). After stretching of the liquid bridge, solution pools are formed on the top and bottom disks, as shown in the binarized image in Figure 1c. Considering the axisymmetric capillary bridge, images of the vertical cross-section of the solution pools are captured. Then, heights, h_T and h_B, of top and bottom solution pools, respectively, are estimated by counting the pixels in the appropriate directions. The truncated sphere method[17] is implemented to calculate the volume of the solution pools: $V_{T,B} = \pi h_{T,B}(3R_0^2 + h_{T,B}^2)/6$. Therefore, the transfer ratio, T_r, is defined in the same way as previous authors[16,17,20,38,39] as $T_r = V_T/(V_T + V_B)$. In the following, every T_r data point and the associated error bar symbolize the average of five experiments and their dispersion, respectively.

EXPERIMENTAL RESULTS AND DISCUSSION

The results consist of a series of experiments that report the T_r for different polymer mass fractions, disk diameters, final heights, and finally different shapes of the initial capillary bridge. The resulting T_r are discussed in terms of morphology of the interface and gravitational drainage.

Effect of Polymer Mass Fraction. The PEO mass fraction is varied, in the aqueous PEO and PEG + PEO solutions, to test its influence on T_r. Experiments are preformed using water, PEG20, PEO, and PEG + PEO solutions. For these experiments, cylindrical-shaped initial liquid bridges are prepared with R_0 = 3 mm and L_0/R_0 = 0.66. Then, the liquid bridges are stretched to L/R_0 = 2 at U = 0.08 m/s. These initial capillary bridges are inside the stability limit curve.[40] The T_r obtained are presented against the PEO mass fraction, w_{PEO}, in Figure 3a. For both the PEO and PEG + PEO solutions, T_r decreases with increasing w_{PEO}. The same can be confirmed from the inset photographs where a smaller top solution pool for PEO2000 solution compared to water can be observed.

Typically, for a viscoelastic liquid bridge, the liquid transfer occurs in two stages. In the first stage, when a liquid bridge is stretched, the minimum radius location along the filament appears and an initial liquid transfer takes place from the bottom to the top disk. When Bo > 1 for R_0 = 3 mm (see Table S2 in the Supporting Information), an initial asymmetry (sagging) decides the primary liquid distribution along the stretched liquid bridge. Hence, when the liquid bridge is stretched, initially, a larger bottom solution pool is formed compared to the top solution pool. However, for PEO and PEG + PEO solutions, solution pools are formed along with a filament that plays a significant role in the second stage of liquid transfer. In this second stage, the liquid is transferred from the top to the bottom solution pool due to gravitational drainage through the filament. As observed in Figure 2b, with increasing w_{PEO}, the filament lasts longer and liquid bridge rupture gets delayed.[32] As a result, there is more time for the gravitational drainage and more liquid is transferred from the top to the bottom solution pool. For a low mass fraction, for both PEO and PEG + PEO solutions, the filament breaks up early and there is less time available for the liquid transfer from the top to the bottom solution pool. Hence, the viscoelastic liquids nearly reproduce the response of PEG20, as reported by Sankaran and Rothstein.[25] Furthermore, for PEG + PEO solutions, the filament lasts longer compared to the PEO solutions. Hence, because of the higher gravitational drainage, lower values of T_r are obtained for the PEG + PEO solutions compared to the PEO solutions. Power law fits are used to capture the change in T_r with w_{PEO}, and the exponents for PEO and PEG + PEO solutions are 0.09 and 0.19, respectively. The larger exponent of the fit for the PEG + PEO solutions than for the PEO solutions suggests that the effect of change in w_{PEO} is higher for the PEG + PEO solutions.

Furthermore, for PEO and PEG + PEO solutions, T_r is plotted as a function of De in Figure 3b. For both solutions, T_r decreases with increasing De. Similar behavior was observed numerically by Lee et al.,[26] where the authors reported that the liquid transferred to the top disk decreases with an increase in De. However, these results were obtained for a combination of the gravure cell at the bottom and a flat plate moving upward. Again, power law fits can be used to represent T_r, and the exponents differ for PEG + PEO solutions (−0.27 for Bo = 1.61) compared to PEO solutions (−0.10 for Bo = 1.48).

Effect of Disk Radius. One of the important parameters of the capillary bridge geometry is the disk radius. To understand the influence of R_0 on T_r, disks of different radii, such as 2, 3, and 4 mm, are tested by keeping other geometric parameters the same. As a result, depending on R_0, the Bond number, Bo, varies from 0.66 to 2.63. For these set of experiments, L_0/R_0 and L/R_0 are kept constant at 0.66 and 2, respectively, whereas the stretching speed, U, is again 0.08 m/s. It can be observed that for all disk radii tested, T_r decreases with De. Additionally, the increase in R_0 as well as Bo globally leads to the decrease in T_r and indicates the effect of gravity. A similar decrease in T_r with R_0 has been reported for water by Zhang et al.[22]

In the photographs of Figure 3b, the stretched liquid bridges with different R_0 are displayed for PEO1000 solution at L/R_0 = 2. With an increase in R_0 from 2 to 4 mm, the shape of the top solution pools weakly changes from convex to concave in the vertical plane, but the shape of the bottom solution pools remains convex. However, the capillary pressure associated to the shape change is dominated by hydrostatic pressure difference (ρgL). In addition, for the largest R_0, the hydrostatic pressure difference overcomes the capillary pressure associated to the mean curvature in the horizontal planes of the top solution pool. Hence, with increasing R_0, more solution is pushed

https://doi.org/10.1021/acs.langmuir.1c01462
Langmuir 2021, 37, 10348−10353

from the top solution pool toward the bottom solution pool due to the increased stretched liquid bridge height (fixed $L/R_0 = 2$). Furthermore, it has been observed that the filament thinning time increases with increasing R_0. Hence, the gravitational drainage through the filament is enhanced by the larger disk radius that results in lower values of T_r. For each Bo, power law fits are again used to capture the change in T_r with De. With increasing Bo, the power law exponents increase from 0.05 to 0.29, suggesting a larger effect of De on higher Bo due to the combined effect of gravity and delayed filament thinning. For each w_{PEO}, T_r decreases linearly with Bo. A reduced plot is shown in the Supporting Information (Figure S1b).

Effect of Final Stretching Height. The effect of the final stretching height on the liquid transfer is explored by varying the final aspect ratio, L/R_0, from 2 to 6. All other geometrical and stretching parameters are kept constant. The minimum value of L/R_0 is limited by the least value of the stretching height required for breaking of the capillary bridge, whereas the maximum value of L/R_0 is limited by the experimental constraints. Two different experimental studies are carried out for the PEG20 and PEO solutions.

PEG20 Solution. The obtained results for the variation of T_r are plotted against L/R_0 in Figure S3 in the Supporting Information. The photographs illustrate different shapes of the capillary bridges formed, just before their breakup, when the top disk is at $L/R_0 = 2$, 4, and 6. The T_r decreases linearly with an increase in the L/R_0. For $L/R_0 = 6$, the breakup occurs close to the top solution pool, compared to the breakup at the middle of the bridge, for $L/R_0 = 2$. This further suggests that after breakup, the liquid transferred to both disks will be nearly the same for $L/R_0 = 2$. However, with increasing L/R_0, as the breakup point moves closer to the top solution pool, more liquid volume will be enclosed below this breakup point and a larger solution pool is formed on the bottom disk. Hence, with increasing final stretching height, less liquid will be transferred to the top disk.

PEO Solutions. The change in T_r for values of $L/R_0 = 2$, 4, and 6 is plotted against De, as shown in Figure 4. For all L/R_0, with the increase in De, T_r decreases. Additionally, for the same De, it can be noted that the increase in L/R_0 leads to the decrease in T_r. This behaviour appears to be more significant for $De > 10$. Hence, for $De > 10$, power law fits of T_r are used for each L/R_0. With increasing L/R_0, the value of the power law exponent increases from 0.07 to 0.12. The location of the necking points, on the liquid bridge, varies with different L/R_0, in a similar manner to PEG20 (see photographs in Figure S3 in the Supporting Information). The length of the filament increases with increasing L/R_0, and hence, a larger liquid volume is enclosed below this necking point. Again, the filament lasts longer with the increase in De, which further helps for the drainage. This combined effect of the location of the necking point and drainage produces smaller values of T_r at higher L/R_0 and De.

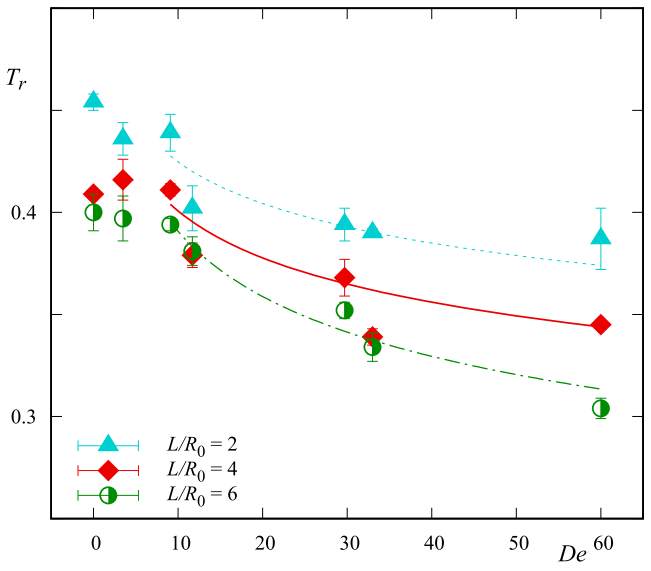

Figure 4. T_r as a function of De for different L/R_0 using PEO solutions. The liquid bridge, formed in between the two disks having $R_0 = 2$ mm is stretched from $L_0/R_0 = 0.66$ to different L/R_0 at $U = 0.08$ m/s.

Effects of stretching speed on liquid transfer are discussed in detail in the Supporting Information, in Figure S4. For PEO solutions, our results show that T_r does not increase significantly with increasing U due to $Ca \leq 0.01$.

Effect of Initial Bridge Shape. The influence of initial bridge shape on liquid transfer is studied by varying the liquid volume introduced with the pipette. This also plays a role in setting the initial liquid contact angles. For a cylindrical-shaped liquid bridge, the liquid volume is $\mathcal{V}$. Then, a dimensionless parameter, $\overline{V}$, is defined as the ratio of the actual liquid volume introduced to $\mathcal{V}$. The cylindrical-shaped liquid bridge, for which $\overline{V} = 1$, and the associated contact angle on the top disk, $\theta_T \simeq 90°$, are illustrated in the inset of Figure 5a. $\overline{V}$ is varied from 0.5 to 1.25, resulting in $55° \lesssim \theta_T \lesssim 115°$. In our experiments, for $\overline{V} < 0.5$ or $\overline{V} > 1.25$, the bridge is found to be unfeasible or unstable.

Four different types of fluids, such as water, PEG20, PEO1000, and PEG20PEO1000, are used to characterize the effect of the initial bridge shape on T_r. The liquid bridges, formed with $R_0 = 2$ mm, are stretched from $L_0/R = 0.66$ to $L/R = 2$ at $U = 0.134$ m/s. The initial bridge shape with the contact angles, $\theta_T < 90°$, at the top disk is similar to those in previous works,[17,18,27,38] where slipping contact lines were observed. However, in our case, the liquid contact lines are pinned for all initial bridge shapes. The aqueous solutions have the tendency to wet the hydrophilic stainless-steel disks. Clearly, PTFE disks would lead to unpinning and sliding of the contact lines, which in turn induce unwanted interface dynamics[1,27] in the present study. The obtained T_r results are plotted against the increasing $\overline{V}$ in Figure 5a. It can be observed that T_r increases with an increase in $\overline{V}$ for water and PEG20. However, for PEO1000 and PEG20PEO1000 viscoelastic solutions, the increase in $\overline{V}$ has exactly the opposite effect, where T_r decreases with an increase in $\overline{V}$.

The effect of the initial bridge shape is further investigated, for PEO1000, by measuring the mid-plane diameter, D_{mid}, of the initial liquid bridge, for $R_0 = 2$ and 3 mm, for all $\overline{V}$ using image analysis. The inset photographs illustrate different shapes of PEO1000 liquid bridges formed for various $\overline{V}$ with $R_0 = 3$ mm when the top disk is at $L/R_0 = 2$. With an increase in $\overline{V}$, a larger filament radius can be observed, which enhances the gravitational drainage through the filament. Note that this filament radius after stretching is related to R_{mid}. Then, T_r is plotted in Figure 5b against the modified Bond number calculated using R_{mid}, that is, $Bo_m = \rho g R_{mid}^2/\sigma$ (see the inset of Figure 5a for a sketch with D_{mid}). Other definitions of the Bond number have been proposed.[41,42] Here, a power law fit is obtained with $T_r \propto Bo_m^{-0.46}$ and a coefficient of determination of 0.92. This results in T_r being proportional to $R_{mid}^{-0.92}$. For $\overline{V} = 1$, it was reported that T_r decreases linearly with Bo (see Figure S1b in the Supporting Information). However, when $\overline{V} \neq 1$, the curvatures controlling the Laplace pressures are changed, while the height, L_0, and thus the hydrostatic pressure, is not. Hence, a physics-based formulation for the Bond number would be

$$Bo^* = \frac{\rho g L_0}{\sigma/R_{mid} + \sigma/\mathcal{R}}$$

$\mathcal{R}$ is the radius in the vertical plane (see the sketch in the inset of Figure 5a), axisymmetric as a first approximation. As $\sigma/\mathcal{R}$ changes sign when $\overline{V}$ varies around 1, $Bo^* \simeq \rho g L_0 R_{mid}/\sigma$. Our results on Bo_m convert into T_r being close to a linear decrease with Bo^*, rather than Bo.

CONCLUSIONS

Liquid transfer for viscoelastic polymer solutions was studied experimentally. Reference results using Newtonian liquids on the effect of the initial and final aspect ratios have shown a

https://doi.org/10.1021/acs.langmuir.1c01462
Langmuir 2021, 37, 10348−10353

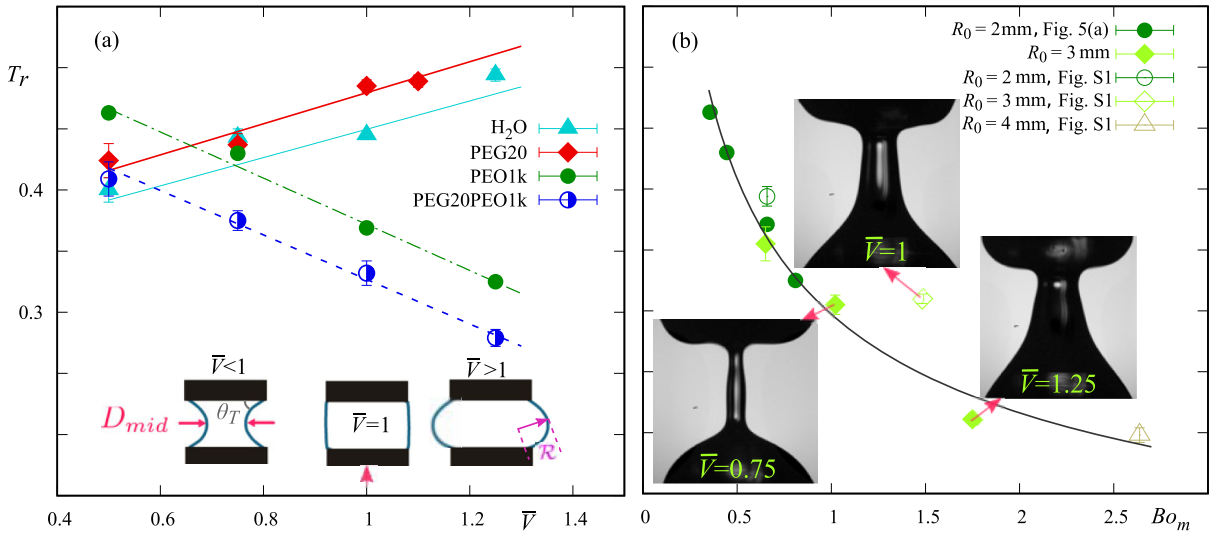

Figure 5. (a) T_r as a function of $\overline{V}$ for Newtonian and viscoelastic solutions. Liquid bridges formed in between two disks having R_0 = 2 mm are stretched from L_0/R_0 = 0.66 to L/R_0 = 2 at U = 0.134 m/s. The liquid volume introduced is varied from 8 to 20 μL ($0.5 < \overline{V} < 1.25$), as illustrated in the inset. (b) T_r as a function of Bo_m for PEO1000 over a range of R_0 and $\overline{V}$. The trend line is a power law fit with $T_r \propto Bo_m^{-0.46}$. The photographs depict stretched liquid bridges for various $\overline{V}$ with R_0 = 3 mm, when the top disk reaches L/R_0 = 2, with arrows indicating the associated data points. $\overline{V}$ = 1 for the points from Figure S1. U = 0.08 m/s, except for data from Figure 5a.

linear decrease of transfer ratio. Then, the cylindrical-shaped liquid capillary bridge, with pinned contact lines between two parallel disks, was stretched for a range of polymer mass fractions. The transfer ratio decreases with Deborah number and can be explained by the gravitational draining enhanced by the delayed filament thinning. The gravitational influence was further studied by using different disk radii, and the results show that transfer ratio decreases for viscoelastic fluids with increasing disk radius, similar to Newtonian fluids. From the printing point of view, smaller values of polymer mass fraction, disk radius, and initial stretching height along with final stretching height should be favored for larger liquid transfer. For non-cylindrical-shaped bridges, the liquid transfer behavior varies sensitively with the liquid volume introduced. Moreover, the behavior of the transfer for Newtonian solutions increases as a function of actual liquid volume introduced and decreases with viscoelastic solutions. Then, the trend for results with PEO1000 follows a power law with $Bo_m^{-0.46}$, where Bo_m is the Bond number computed from the initial mid-plane radius. Another Bond number, Bo^*, with explicit curvatures could be used but can have negative values. Hence, for future studies on transfer ratio, the experimentally tractable Bo_m based on actual radius R_{mid} is suggested.

■ ASSOCIATED CONTENT

Supporting Information

The Supporting Information is available free of charge at https://pubs.acs.org/doi/10.1021/acs.langmuir.1c01462.

Details of the fluid properties including dimensionless numbers and additional results on T_r for effect of R_0 and Bo; effect of initial aspect ratio, L_0/R_0; effect of final aspect ratio, L/R_0; and effect of stretching velocity (PDF)

■ AUTHOR INFORMATION

Corresponding Author

Jorge Peixinho − *Laboratoire PIMM, CNRS, Arts et Métiers Institute of Technologie, Cnam, Paris 75013, France; LOMC, CNRS and Université Le Havre Normandie, Le Havre 76600, France;* orcid.org/0000-0003-0850-3406; Email: jorge.peixinho@ensam.eu

Authors

Hrishikesh Pingulkar − *LOMC, CNRS and Université Le Havre Normandie, Le Havre 76600, France*

Olivier Crumeyrolle − *LOMC, CNRS and Université Le Havre Normandie, Le Havre 76600, France*

Complete contact information is available at: https://pubs.acs.org/10.1021/acs.langmuir.1c01462

Notes

The authors declare no competing financial interest.

■ ACKNOWLEDGMENTS

The authors thank M.-C. Renoult for discussions on the downward stretching and M. Grisel for access to a rheometer with double-wall concentric cylinders. Partial funding for this research was provided by the project BIOENGINE, which was co-financed by the European Union with the European Regional Development Fund and the Région Normandie, the French Agence Nationale de la Recherche and LabEx EMC3 through the project IBOASD (grant no. ANR-10-LABX-09-01), and the Université Le Havre Normandie (support of H.P.).

■ REFERENCES

(1) Kumar, S. Liquid transfer in printing processes: liquid bridges with moving contact lines. *Annu. Rev. Fluid. Mech.* **2015**, *47*, 67−94.

(2) Gutiérrez, J. A. F.; Moura, M. J. B.; Carvalho, M. S. Dynamics of viscoelastic flow through axisymmetric constricted microcapillary at high elasticity number. *J. Non-Newtonian Fluid Mech.* **2020**, *286*, 104438.

(3) Karim, A. M.; Suszynski, W. J.; Pujari, S.; Francis, L. F.; Carvalho, M. S. Delaying breakup and avoiding air entrainment in curtain coating using a two-layer liquid structure. *Chem. Eng. Sci.* **2020**, *213*, 115376.

(4) Montanero, J. M.; Ponce-Torres, A. Review on the the dynamics of isothermal liquid bridges. *Appl. Mech. Rev.* **2020**, *72*, 010803.
(5) Sekine, T.; Sugano, R.; Tashiro, T.; Sato, J.; Takeda, Y.; Matsui, H.; Kumaki, D.; Dos Santos, F. D.; Miyabo, A.; Tokito, S. Fully printed wearable vital sensor for human pulse rate monitoring using ferroelectric polymer. *Sci. Rep.* **2018**, *8*, 4442.
(6) Park, J.-U.; Hardy, M.; Kang, S. J.; Barton, K.; Adair, K.; Mukhopadhyay, D. k.; Lee, C. Y.; Strano, M. S.; Alleyne, A. G.; Georgiadis, J. G.; Ferreira, P. M.; Rogers, J. A. High-resolution electrohydrodynamic jet printing. *Nat. Mater.* **2007**, *6*, 782−789.
(7) Krebs, F. C. Fabrication and processing of polymer solar cells: A review of printing and coating techniques. *Sol. Energy Mater. Sol. Cells* **2009**, *93*, 394−412.
(8) Grilli, S.; Coppola, S.; Vespini, V.; Merola, F.; Finizio, A.; Ferraro, P. 3D lithography by rapid curing of the liquid instabilities at nanoscale. *Proc. Natl. Acad. Sci. U.S.A.* **2011**, *108*, 15106−15111.
(9) Goldin, M.; Yerushalmi, J.; Pfeffer, R.; Shinnar, R. Breakup of a laminar capillary jet of a viscoelastic fluid. *J. Fluid Mech.* **1969**, *38*, 689−711.
(10) Oliveira, M. S. N.; Yeh, R.; McKinley, G. H. Iterated stretching, extensional rheology and formation of beads-on-a-string structures in polymer solutions. *J. Non-Newtonian Fluid Mech.* **2006**, *137*, 137−148.
(11) Tirtaatmadja, V.; McKinley, G. H.; Cooper-White, J. J. Drop formation and breakup of low viscosity elastic fluids: Effects of molecular weight and concentration. *Phys. Fluids* **2006**, *18*, 043101.
(12) Dinic, J.; Jimenez, L. N.; Sharma, V. Pinch-off dynamics and dripping-onto-substrate (DoS) rheometry of complex fluids. *Lab Chip* **2017**, *17*, 460−473.
(13) Ponce-Torres, A.; Vega, E. J.; Castrejón-Pita, A. A.; Montanero, J. M. Smooth printing of viscoelastic microfilms with a flow focusing ejector. *J. Non-Newtonian Fluid Mech.* **2017**, *249*, 1−7.
(14) Pingulkar, H.; Peixinho, J.; Crumeyrolle, O. Drop dynamics of viscoelastic filaments. *Phys. Rev. Fluids* **2020**, *5*, 011301.
(15) Chadov, A. V.; Yakhnin, E. D. Investigation of the transfer of a liquid from one solid-surface to another. 1. Slow transfer-method of approximate calculation. *Colloid J. USSR* **1979**, *41*, 700−703.
(16) Yakhnin, E. D.; Chadov, A. V. Investigation of the transfer of a liquid from one solid-surface to another. 2. Dynamic transfer. *Colloid J. USSR* **1983**, *45*, 1034−1039.
(17) Kang, H. W.; Sung, H. J.; Lee, T.-M.; Kim, D.-S.; Kim, C.-J. Liquid transfer between two separating plates for micro-gravure-offset printing. *J. Micromech. Microeng.* **2008**, *19*, 015025.
(18) Ahmed, D. H.; Sung, H. J.; Kim, D.-S. Simulation of non-Newtonian ink transfer between two separating plates for gravure-offset printing. *Int. J. Heat Fluid Flow* **2011**, *32*, 298−307.
(19) Chen, H.; Tang, T.; Amirfazli, A. Effects of surface wettability on fast liquid transfer. *Phys. Fluids* **2015**, *27*, 112102.
(20) Huang, C.-H.; Carvalho, M. S.; Kumar, S. Stretching liquid bridges with moving contact lines: comparison of liquid-transfer predictions and experiments. *Soft Matter* **2016**, *12*, 7457−7469.
(21) de Gennes, P. G. Wetting: statics and dynamics. *Rev. Mod. Phys.* **1985**, *57*, 827−863.
(22) Zhang, X.; Padgett, R. S.; Basaran, O. A. Nonlinear deformation and breakup of stretching liquid bridges. *J. Fluid Mech.* **1996**, *329*, 207−245.
(23) Dodds, S.; Carvalho, M. d. S.; Kumar, S. Stretching and slipping of liquid bridges near plates and cavities. *Phys. Fluids* **2009**, *21*, 092103.
(24) Dodds, S.; Carvalho, M.; Kumar, S. Stretching liquid bridges with moving contact lines: The role of inertia. *Phys. Fluids* **2011**, *23*, 092101.
(25) Sankaran, A. K.; Rothstein, J. P. Effect of viscoelasticity on liquid transfer during gravure printing. *J. Non-Newtonian Fluid Mech.* **2012**, *175−176*, 64−75.
(26) Lee, J. A.; Rothstein, J. P.; Pasquali, M. Computational study of viscoelastic effects on liquid transfer during gravure printing. *J. Non-Newtonian Fluid Mech.* **2013**, *199*, 1−11.
(27) Wu, J.-T.; Carvalho, M. S.; Kumar, S. Effects of shear and extensional rheology on liquid transfer between two flat surfaces. *J. Non-Newtonian Fluid Mech.* **2019**, *274*, 104173.
(28) Christanti, Y.; Walker, L. M. Surface tension driven jet break up of strain-hardening polymer solutions. *J. Non-Newtonian Fluid Mech.* **2001**, *100*, 9−26.
(29) Tirel, C.; Renoult, M.-C.; Dumouchel, C.; Lisiecki, D.; Crumeyrolle, O.; Mutabazi, I. Multi-scale analysis of a viscoelastic liquid jet. *J. Non-Newtonian Fluid Mech.* **2017**, *245*, 1−10.
(30) Rodd, L. E.; Scott, T. P.; Cooper-White, J. J.; McKinley, G. H. Capillary break-up rheometry of low-viscosity elastic fluids. *Appl. Rheol.* **2005**, *15*, 12−27.
(31) Deblais, A.; Velikov, K. P.; Bonn, D. Pearling instabilities of a viscoelastic thread. *Phys. Rev. Lett.* **2018**, *120*, 194501.
(32) Bazzi, M. S.; Carvalho, M. S. Effect of viscoelasticity on liquid sheet rupture. *J. Non-Newtonian Fluid Mech.* **2019**, *264*, 107−116.
(33) Gaillard, A.; Roché, M.; Lerouge, S.; Gay, C.; Lebon, L.; Limat, L. Viscoelastic liquid curtains: experimental results on the flow of a falling sheet of polymer solution. *J. Fluid Mech.* **2019**, *873*, 358−409.
(34) Karim, A. M.; Suszynski, W. J.; Griffith, W. B.; Pujari, S.; Francis, L. F.; Carvalho, M. S. Effect of viscoelasticity on stability of liquid curtain. *J. Non-Newtonian Fluid Mech.* **2018**, *257*, 83−94.
(35) Layec, Y.; Layec-Raphalen, M.-N. Instability of dilute poly(ethylene-oxide) solutions. *J. Phys., Lett.* **1983**, *44*, 121−128.
(36) Bird, R. B.; Armstrong, R. C.; Hassager, O. *Dynamics of Polymeric Liquids. Vol. 1: Fluid Mechanics*; Wiley-Interscience, 1987.
(37) Bhat, P. P.; Appathurai, S.; Harris, M. T.; Pasquali, M.; McKinley, G. H.; Basaran, O. A. Formation of beads-on-a-string structures during break-up of viscoelastic filaments. *Nat. Phys.* **2010**, *6*, 625−631.
(38) Chen, H.; Tang, T.; Amirfazli, A. Liquid transfer mechanism between two surfaces and the role of contact angles. *Soft Matter* **2014**, *10*, 2503−2507.
(39) Tourtit, Y.; Gilet, T.; Lambert, P. Rupture of a liquid bridge between a cone and a plane. *Langmuir* **2019**, *35*, 11979−11985.
(40) Bezdenejnykh, N. A.; Meseguer, J.; Perales, J. M. Experimental analysis of stability limits of capillary liquid bridges. *Phys. Fluids* **1992**, *4*, 677−680.
(41) Mazzone, D. N.; Tardos, G. I.; Pfeffer, R. The effect of gravity on the shape and strength of a liquid bridge between two spheres. *J. Colloid Interface Sci.* **1986**, *113*, 544−556.
(42) Willett, C. D.; Adams, M. J.; Johnson, S. A.; Seville, J. P. K. Capillary bridges between two spherical bodies. *Langmuir* **2000**, *16*, 9396−9405.

https://doi.org/10.1021/acs.langmuir.1c01462
Langmuir 2021, 37, 10348−10353

Supporting Information for

Liquid Transfer for Viscoelastic Solutions

Hrishikesh Pingulkar,[†] Jorge Peixinho,[*,‡,†] and Olivier Crumeyrolle[,†]

†*LOMC, CNRS and Université Le Havre Normandie, Le Havre, France*

‡*Laboratoire PIMM, CNRS, Arts et Métiers Institute of Technologie, Cnam, Paris, France*

E-mail: jorge.peixinho@ensam.eu

The Tables S1 and S2 below detail the measured fluid properties and the associated dimensionless numbers, respectively. Figures S1, S2, S3 and S4 present additional results on T_r for (i) the effect of the plate radius, R_0, and Bo, (ii) the effect of the initial aspect ratio, L_0/R_0, (iii) the effect of the final aspect ratio, L/R_0, and (iv) the effect of the stretching velocity, U. In these experiments, the initial capillary bridge is cylindrical, *i.e.* $\overline{V} = 1$.

Solutions Used and Properties

The experiments were performed in a room with air conditioning and a thermal bath (from ThermoFisher scientific) is used to ensure the environment of the capillary bridge remains at 20°C. Densities, ρ, of the solutions were measured with a portable density meter from Anton Paar, which has a resolution 0.1 mg/cm^3. Surface tensions, σ, of solutions were measured with Kruss drop shape analyser (series 100), with a resolution 0.01 mN/m. Three types of solutions were prepared. In the first type, to make highly viscous solution, PEG was added to degassed water. In the second type, to have highly elastic solution, PEO was mixed with degassed water. In the third type, both PEO and PEG solutions are mixed together. The mixed solutions are kept for at least 72 hours to ensure complete mixing of the polymers.

Table S1: Properties of the solutions

Abbreviation	w_{PEG} wt. %	w_{PEO} wppm	ρ kg/m^3	σ mN/m	η_0 [a] Pa.s	λ [b] s
PEG20	20	0	1032.5	57	0.034	-
PEO100	0	100	997	59	0.0011	0.041
PEO250	0	250	997.1	59	0.0013	0.106
PEO800	0	800	997.3	59	0.0010	0.135
PEO1000	0	1000	997.3	59	0.006	0.344
PEO1500	0	1500	997.5	59	0.054	0.382
PEO2000	0	2000	997.6	59	0.039	0.696
PEG20PEO100	20	100	1032.8	56	0.160	0.535
PEG20PEO250	20	250	1033.4	56	0.165	1.350
PEG20PEO400	20	400	1033.4	56	0.166	1.367
PEG20PEO800	20	800	1033.6	56	0.170	2.396
PEG20PEO1000	20	1000	1033.6	56	0.771	2.952
PEG20PEO2000	20	2000	1033.4	56	1.682	3.580

[a]The zero shear viscosities, η_0, were obtained by fitting the Carreau equation to the shear rheology data with the infinite viscosity prescribed to the solvent one.

[b]The viscoelastic relaxation times, λ, were obtained by fitting the exponential thinning to CaBER data with $D_0 = 6$ mm, $L_0 = 2$ mm, $L = 6$ mm and $U = 0.08$ m/s.

Table S2: Dimensionless numbers for three plate used: $Bo = \rho g R_0/\sigma$, $De = \lambda/\tau_R$, $Oh = \tau_v/\tau_R$ where $\tau_R = \sqrt{\rho R_0^3/\sigma}$ and $\tau_v = \eta_0 R_0/\sigma$.

Abbreviation	$R_0 = 2$ mm			$R_0 = 3$ mm			$R_0 = 4$ mm		
	Bo	De	Oh	Bo	De	Oh	Bo	De	Oh
PEG20	0.70	-	0.10	1.59	-	0.08	2.82	-	0.07
PEO100	0.66	3.5	$\approx 10^{-3}$	1.48	1.9	$\approx 10^{-3}$	2.63	1.2	$\approx 10^{-3}$
PEO250	0.66	9.1	$\approx 10^{-3}$	1.48	4.9	$\approx 10^{-3}$	2.63	3.2	$\approx 10^{-3}$
PEO800	0.66	11.7	0.03	1.48	6.3	0.02	2.63	4.1	0.02
PEO1000	0.66	29.7	0.02	1.48	16.1	0.01	2.63	10.5	0.01
PEO1500	0.66	33.0	0.16	1.48	17.9	0.13	2.63	11.7	0.11
PEO2000	0.66	60.0	0.11	1.49	32.7	0.09	2.64	21.2	0.08
PEG20PEO100	0.72	44.2	0.47	1.62	24.0	0.38	2.88	15.6	0.33
PEG20PEO250	0.72	111.7	0.48	1.61	60.8	0.39	2.87	39.5	0.34
PEG20PEO400	0.71	113.4	0.48	1.60	61.7	0.40	2.85	40.1	0.34
PEG20PEO800	0.72	198.4	0.50	1.61	108.0	0.41	2.86	70.1	0.35
PEG20PEO1000	0.72	224.0	2.26	1.61	132.8	1.84	2.87	86.3	1.60
PEG20PEO2000	0.72	296.4	4.91	1.61	161.3	4.01	2.86	104.8	3.48

The properties of the solutions are listed in Table S1. Taking into account the wide range of parameter, several dimensionless number are presented in Table S2.

In the following, we present the effects of various parameters on T_r.

Radius: R_0

To understand influence of the plate diameter on T_r, three plates diameters with $R_0 = 2$, 3 and 4 mm, are tested. A liquid bridge, formed in-between the two plates, is stretched from $L_0/R_0 = 0.66$ to $L/R_0 = 2$ at $U = 0.08$ m/s. Figure S1 displays T_r as a function of the disk radius for different liquids. For all solutions, T_r decreases with R_0.

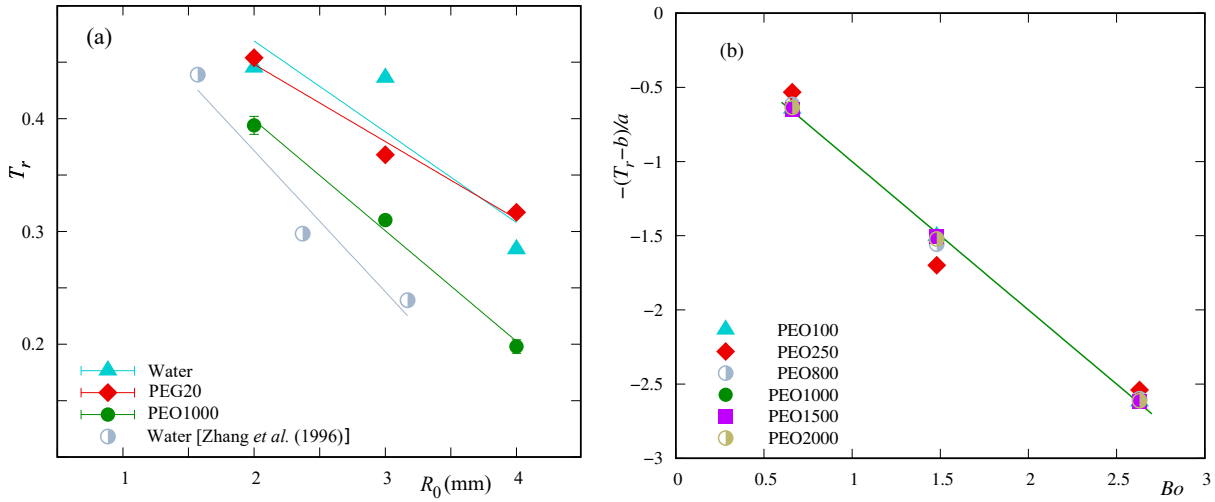

Figure S1: (a) T_r as a function of R_0 with $\overline{V} = 1$. The water results are compared with Zhang et al.[1] with lower stretching speed, $U = 0.006$ m/s, and higher $L_0/R_0 = 2$. The lines represent linear fits. (b) Reduced T_r versus Bo for PEO solutions. For each w_{PEO}, a unique couple (a, b) is found by a linear regression, $T_r = -a\,Bo + b$, with the coefficient of determination ranging from 0.9643 to 0.9998.

Initial Aspect Ratio: L_0/R_0

The influence of the initial capillary bridge height, L_0, on T_r is studied by varying the initial aspect ratio, L_0/R_0, from 0.2 to 2, for PEG20 solution. The obtained results for T_r are plotted against L_0/R_0 in Figure S2. With increasing L_0/R_0, T_r decreases and this trend has been previously observed numerically for a Newtonian liquid by Huang et al..[2] In their study, the contact line on the top plate was pinned and the contact line on the bottom

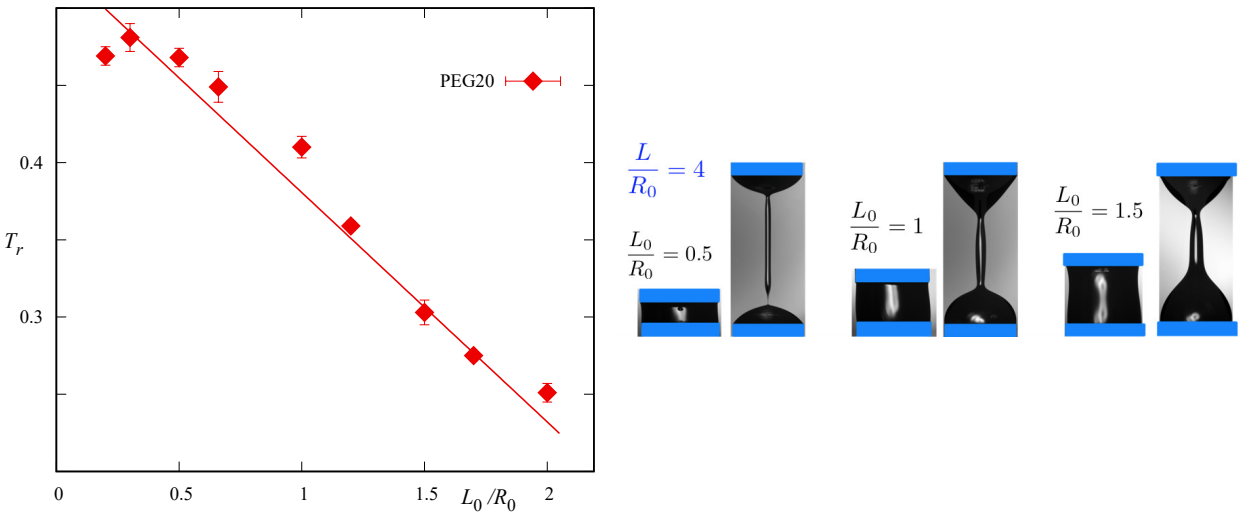

Figure S2: Effect of the initial aspect ratio, L_0/R_0, on the transfer ratio T_r, for PEG20. The solid red line represents a linear fit. All experiments are conducted with $D_0 = 4$ mm and $U = 0.134$ m/s. The images represent the initial and breakup instant for different runs.

plate was free to slip. However, in the present study, the contact lines on both plates are fixed and more number of data points are reported. According to Rodd et al.,[3] for a static liquid bridge, in order to keep the initial configuration close to a cylindrical shape (without sagging), $L_0/R_0 \leq 1/\sqrt{Bo}$. For the liquid bridge of PEG20 solution with $R_0 = 2$ mm and $Bo = 0.70$, this critical L_0/R_0 is 1.19. Hence, in the present study, for $L_0/R_0 > 1.2$, instabilities are caused by the imbalance between gravity and capillarity. With increasing L_0/R_0, gravitational forces overcome the capillary forces and axial sagging in the direction of gravity is observed. Therefore, the liquid bridge becomes non-cylindrical and bulged shaped closer to the bottom plate. Transition of the initial capillary bridge from the cylindrical shape to the non-cylindrical (bulged) shape due to increase in L_0/R_0 can be seen in photographs presented in Figure S2. For $L_0/R_0 \leq 0.5$, when the top plate is stretched upwards, the liquid bridge breakup first occurs closer to the bottom solution pool. However, when the top plate is stretched upwards, for $L_0/R_0 > 0.5$, the breakup point moves towards the top solution pool. Additionally, for $L_0/R_0 > 1.2$, when the liquid bridge is stretched, the bulge shaped liquid (on the bottom plate) appears. Therefore, with increasing L_0/R_0, smaller solution pool is formed on the top plate and the T_r decreases.

Final Aspect Ratio, L/R_0

To understand the effect of the final stretching height on T_r, the final aspect ratio, L/R_0, is varied from 2 to 6, for PEG20 solutions. The minimum of L/R_0 is limited due to the least value of the stretching height, required for breaking of the capillary bridge, whereas the maximum value of L/R_0 is limited by the experimental constraints. The different values of L/R_0 are obtained by only varying the final stretching height, L, and keeping all other parameters constant, such as $D_0 = 4$ mm and $L_0/R_0 = 0.66$. The results are presented in Figure S3.

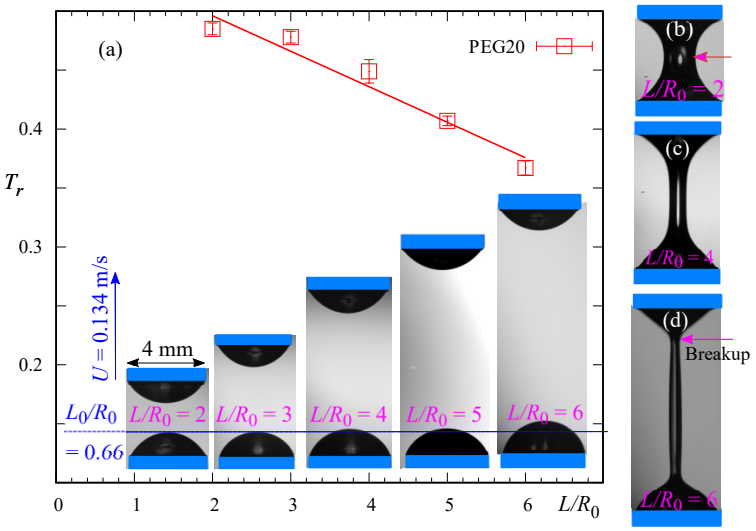

Figure S3: (a) Effect of the final aspect ratio, L/R_0, on the transfer ratio, T_r, for PEG20 solution. The insets are the photographs illustrating the solution pools formed on the plates, for the different final stretching heights, with L/R_0 from 2 to 6 and $D_0 = 4$ mm. The dashed blue line shows the initial stretching height, for which $L_0/R_0 = 0.66$, for all the experiments. The blue arrow indicates the stretching direction of the initial capillary bridge, with $U = 0.134$ m/s. The solid red line is the linear fit, with the coefficient of determination of 0.96. Photographs (b), (c) and (d) depict the liquid capillary bridges, for PEG20, just before their rapture, pulled to the final stretching heights, for $L/R_0 = 2$, 4 and 6, respectively.

Stretching Speed: U

The effect of stretching speed, U, on transfer ratio, T_r, is studied by gradually varying U, from 1 to 134 mm/s for PEO1000 and PEG20 solutions. The obtained results are plotted with T_r as a function of U, in Figure S4(a). The increase in liquid transfer to the top plate with

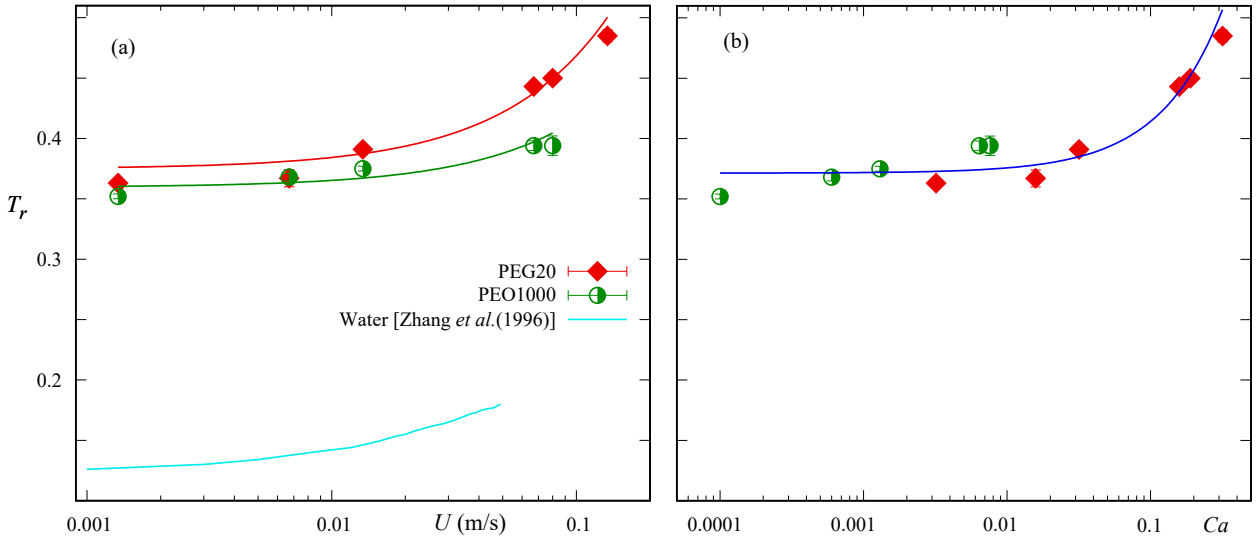

Figure S4: (a) Effect of stretching speed, U, (b) Capillary number, Ca, on transfer ratio, T_r for PEG20 and PEO1000 solutions. $L_0/R_0 = 0.66$ and $L/R_0 = 2$ with the $D_0 = 4$ mm. Thick lines in denote the linear fits.

increasing stretching speed was observed for Newtonian fluids.[1,2,4–6] The results obtained are compared with Zhang et al.[1] and the similar trend of increase in T_r with increasing U is reported. It is recalled that these authors have pinned contact lines similar to the present study and different geometrical properties of liquid bridges: $R_0 = 1.6$ mm and $L_0/R_0 = 2$. However, irrespective of geometrical properties (pinned or moving contact lines), for both Newtonian and viscoelastic solutions, the liquid transferred to the top plate increases with increasing U. For further analysis, the capillary numbers, $Ca = \eta_0 U/\sigma$, are used. The transfer ratios are plotted against Ca, as shown in Figure S4(b). For both solutions, TR increases with increasing Ca. For all the values of Ca, linear regression is used to capture this trend. The change in T_r with Ca can be distinguished in three regimes. These regimes have been previously described using stretching speed[4,5,7] and capillary numbers[2] for moving contact lines and Newtonian fluids. In the present study, we could only achieve the first two regimes because of experimental limitations.

References

(1) Zhang, X.; Padgett, R. S.; Basaran, O. A. Nonlinear deformation and breakup of stretching liquid bridges. *J. Fluid Mech.* **1996**, *329*, 207–245.

(2) Huang, C.-H.; Carvalho, M. S.; Kumar, S. Stretching liquid bridges with moving contact lines: comparison of liquid-transfer predictions and experiments. *Soft Matter* **2016**, *12*, 7457–7469.

(3) Rodd, L. E.; Scott, T. P.; Cooper-White, J. J.; McKinley, G. H. Capillary break-up rheometry of low-viscosity elastic fluids. *Appl. Rheol.* **2005**, *15*, 12–27.

(4) Chadov, A. V.; Yakhnin, E. D. Investigation of the transfer of a liquid from one solid-surface to another. 1. Slow transfer-method of approximate calculation. *Colloid J. USSR* **1979**, *41*, 700–703.

(5) Yakhnin, E. D.; Chadov, A. V. Investigation of the transfer of a liquid from one solid-surface to another. 2. Dynamic transfer. *Colloid J. USSR* **1983**, *45*, 1034–1039.

(6) Chen, H.; Tang, T.; Amirfazli, A. Effects of surface wettability on fast liquid transfer. *Phys. Fluids* **2015**, *27*, 112102.

(7) Chen, H.; Tang, T.; Amirfazli, A. Liquid transfer mechanism between two surfaces and the role of contact angles. *Soft Matter* **2014**, *10*, 2503–2507.